RGNZ/MGPB

Revealing the subsurface of the southwestern part of the Camplong active fault, West Timor, Indonesia by applying audio-frequency magnetotelluric data inversion

Rudarsko-geološko-naftni zbornik
(The Mining-Geology-Petroleum Engineering Bulletin)
DOI: 10.17794/rgn.2026.1.5

Preliminary communication

Febty Febriani[1]*, Cinantya Nirmala Dewi[1], Gusti Muhammad Lucki Junursyah[2], Herry Zardak Kotta[3], Titi Anggono[1], Syuhada[1], Mohamad Ramdhan[1], Faiz Muttaqy[1], Mohammad Hasib[1], Aditya Dwi Prasetio[1], Wiko Setyonegoro[4]

[1]Research Center for Geological Disaster, National Research and Innovation Agency (BRIN), Kawasan Sains dan Teknologi (KST) B.J. Habibie, Jl. Raya Puspiptek, Setu, Tangerang Selatan, Banten, Indonesia, 15314.

[2]Center for Geological Survey, Geological Agency, Jl. Diponegoro No.57, Bandung, Jawa Barat, Indonesia, 40122.

[3]Faculty of Science and Engineering, Nusa Cendana University, Jl. Adisucipto Penfui, Kupang, East Nusa Tenggara, Indonesia, 31201.

[4]Research Center for Deep Sea, National Research and Innovation Agency (BRIN), Kawasan Sains dan Teknologi (KST) B.J. Habibie, Jl. Raya Puspiptek, Setu, Tangerang Selatan, Banten, Indonesia, 15314.

Abstract

Geologically, three active faults exist in West Timor, East Nusa Tenggara (NTT) Province, Indonesia, namely the Babau, Camplong, and Atambua faults. The audio-frequency magnetotelluric (AMT) data is used to model the electrical subsurface of the Camplong Fault's southwestern part. The AMT profile that comprised 15 AMT observation points over a length of 26 km running in an NW–SE direction was subjected to a phase tensor analysis. The results suggest that the studied area has a regional strike of N25°E and that 2-D inverse modelling on the AMT profile was possible. The inverse modelling result indicates the presence of two conductive boundaries (C1: $\rho \leq 5$ Ωm and C2: $\rho \leq 5$ Ωm) in the central and the southeastern parts of the AMT profile that separates the R1 (ρ = 10–50 Ωm) and R2 (ρ = 10–50 Ωm) as well as R2 and R3 (ρ = 5-100 Ωm) zones, respectively. The R1, R2, and R3 are located in the northwestern, central and southeastern parts, respectively. We suggest that the C2 is possibly the damaged zone of the fault in this study area. We also conducted forward modelling and examined the seismic activity and geological background, the results of which aligned with the inverse modelling.

Keywords:
fault zone; earthquake; audio-frequency magnetotelluric; east nusa tenggara; subsurface model

1. Introduction

Timor Island is located in the eastern part of Indonesia. It is approximately 500 kilometers north of Australia and 1,700 kilometers west of Bali Island, separated by the Timor Sea. The island is divided politically into East Timor and West Timor. East Timor is officially recognized as the Democratic Republic of Timor-Leste, while West Timor is as part of Indonesia's East Nusa Tenggara (NTT) Province.

It is also situated within the Banda arc transition zone and was formed as part of the intact Australia Craton before the Miocene era. The tectonic transition zone is characterized by a shift in tectonic processes, transitioning from the Indo-Australian Plate's subduction along the Java Trench in the western part to the continental-island arc's collision along the active volcanic Banda arc in the eastern part (**Powel, 1976**). The Banda arc runs eastward from the island of Flores to the islands of Alor and Wetar. The Banda forearc system consists of Timor Island in the southern arc along the islands of Savu and Rote to the west. To the south of the Banda arc lies the Australian North West Shelf, which is thought to be a continental plate created during the Jurassic breakup of eastern Gondwana (**Powel, 1976**).

Timor Island consists of deformed sediments from the outer margin of the Australian continental plate (**Jacobson and Sani, 1993**). The Banda Sea lies along the northern part of Timor Island, with the Timor Trough in the southern part. The trough extends south–southeast and is 2,000 meters bathymetric deep (**Špičák et al., 2013**). It represents the sea-floor trace of the north dipping subduction zone as a result of the northward movement of the Australian continental plate beneath Timor Island. The structural features on Timor Island include a series of thin-skinned, imbricated thrust sheets forming a foreland fold–thrust system (**Jacobson and Sani, 1993**).

* Corresponding author: Febty Febriani
e-mail address: febt001@brin.go.id; febty82@gmail.com
Received: 4 June 2025. Accepted: 16 July 2025.
Available online: 2 January 2026

The Savu Sea, and Savu and Roti islands lie to the west of Timor Island. The tectonic setting at the Savu basin on Timor Island's western part is very complex. The subduction zone bends southwards close to Sumba Island and continues eastward in a shallow trench. Timor Island sits between the arc and the trench, which are generally considered to form an accretionary complex (**Chamalaun and Grady, 1978; Barber, 1978; Barber and Brown, 1988; Varekam et al., 1989; Charlton et al., 1991**). To the east of Timor Island are the islands of Leti, Kisar, Babar, the Kai Kecil and the Tanimbar Archipelago. They are all part of the Banda outer arc, a geological feature created through the collision between the Eurasian and Indo-Australian plates (**Jacobson and Sani, 1993**).

In addition, the area is a seismically active region. It has been suggested that the Timor Trough is a representation of the oblique convergence between the plate boundary (**DeMets et al., 2010**). At the Timor Trough, the estimated convergence rate is approximately 15 mm/year (**Bock et al., 2003**). **Charlton (2002)** suggested that Timor Island comprises a fold and thrust belt where the Australian margin has been thrust southward. **Villeneuve et al. (2013)** carried out an investigation using geochemical analysis and K–Ar dating. They considered the recent structure in Timor Island to have resulted from tectonic events throughout the Late Oligocene, Late Early Pliocene, and Late Pliocene–Early Pleistocene epochs.

As one of geophysical techniques, the audio-frequency magnetotelluric (AMT) is a part of the magnetotelluric method that uses the audio frequency band to investigate the subsurface condition of hydrocarbon zones, geothermal areas, volcanoes, and inland-earthquake-generating fault zones (**e.g. Honkura et al., 2000; Ogawa et al., 2001; Newman et al., 2008; Ingham et al., 2009; Aizawa et al., 2014; Yamaya et al., 2013; Febriani et al., 2019; Widarto et al., 2022; Daud et al., 2023; Junian & Grandis, 2023**). It has the capability to penetrate from shallow depths in the Earth's crust to few kilometres of the upper earth's crust because it relies on naturally occurring electromagnetic sources, operating within a range of frequency spanning from 0.1 to 2,000 Hz (**Vozoff 1991; Simpson and Bahr, 2005**). The method can determine the phase and apparent resistivity beneath a study area by measuring the electric (Ex, Ey) and magnetic field components (Hx, Hy). Thus, it is possible to image the distribution of conductive and resistive zones in a study area by employing 2-D or 3-D subsurface modelling.

Concerning the examination of inland-earthquake-generating fault zones, previous studies have shown that this method can investigate the borders between the conductive and resistive zones, which relates to the region of the fault zone in a study area (**e.g. Oshiman et al., 2002; Tank et al., 2005; Kaya et al., 2013; Boonchaisuk et al., 2017; Marti el al., 2020; Usui et al., 2021; Widarto et al., 2022; Kim et al., 2023**). Furthermore, combined with the seismicity distribution of a study area, it is possible to reveal the low and high resistivity zones as well as the earthquake epicenter distribution in these zones.

The latest version of the map of all active faults in Indonesia (scale 1:5,000,000) was released in 2021 by the Center for Geological Survey of the Geological Agency, Ministry of Energy and Mineral Resources of the Republic of Indonesia (**Soehaimi et al., 2021**). They suggested three active faults in West Timor, namely the Babau, Camplong, and Atambua fault segments. The Babau Fault is situated in the southwestern part of West Timor and has a northwest–southeast (NW–SE) orientation. The Camplong Fault is located in the center of West Timor, while the Atambua Fault lies in the northeastern part.

We focus our study on the active fault in eastern Indonesia, notably around West Timor, since it remains poorly reported. We investigated the subsurface of the southwestern part of the Camplong Fault using the AMT method to reveal the electrical resistivity imaging of the subsurface of the Camplong Fault and obtain better knowledge related to the subsurface of the fault. Furthermore, this knowledge will be employed to help reduce the risk of future disasters in West Timor.

2. Geological Background

The initiation of the collision in Timor can be traced back to the Latest Miocene period (**Harris, 2011**). The development of the Gondwana Sequence duplex occurred as a product of the collision, overlain by the folded and uplifted Banda Terrain, serving as Timor's tectonic lid (**Harris, 2011**). The Banda Terrane constitute the Mutis/Lolotoi Metamorphic Complex and its sedimentary cover, like the Palelo Group and Metan Formation (**Harris, 2006**). Although the dominance of this sequence is evident in the majority of Timor's northern regions, several studies (including this study, in **Figure 1b**) documented the presence of Banda Terrane rocks on the southern part of Timor's central basin with several indication of the Palelo Group sedimentary cover (**Rosidi et al., 1979; Sawyer et al., 1993; Charlton and Titu-Eki, 2023**). This metamorphic complex may be interpreted as the differentiated Australian continental margin basement (**Charlton and Titu-Eki, 2023**).

Figure 1 indicates the study area's location, which is found in West Timor, East Nusa Tenggara Province, Indonesia. **Figure 1b** presents the dominant geological background in the surrounding study area, comprising limestone, alluvium, ultrabasic rocks, and the Ofu, Batuputih, Bobonaro, Aitutu, Maubise, and Noele formations.

The Ofu Formation generally consists of deformed limestones and possibly represents the local deformation product in the Kolbano area (**Keep and Haig, 2010**). The Ofu Formation shares the same characteristics as the Batuputih Formation. Both were made up of white

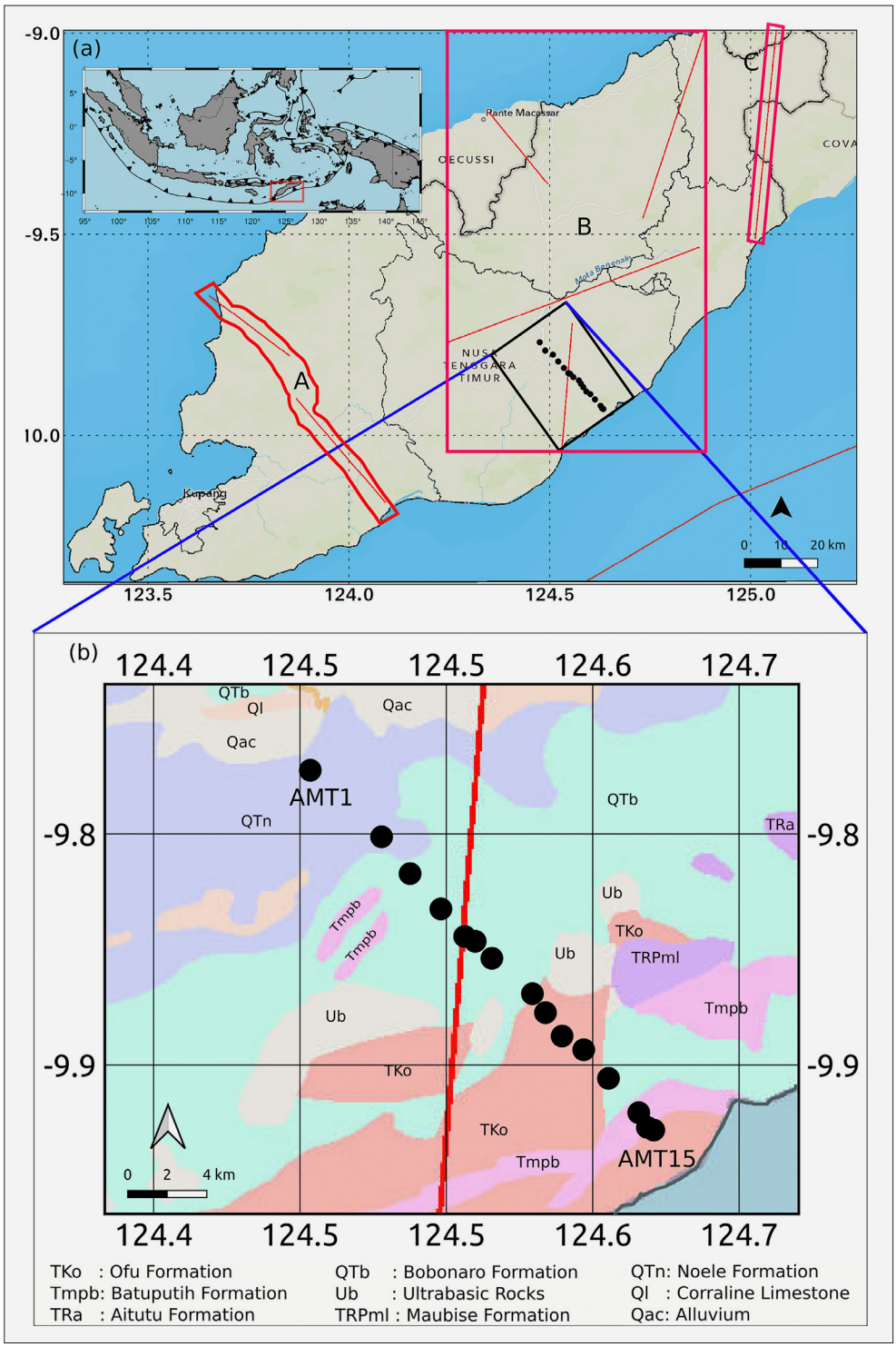

Figure 1. (a) Location of research area in West Timor. The fault segments (red square) proposed by **Soehaimi et al. (2021)** are labelled as A (the Babau Fault segment), B (the Camplong Fault segment), and C (the Atambua Fault segment). The black dots are the AMT observation points. (b) The geological map of the research area passed by the southwestern part of the Camplong Fault (red line) issued by the **Indonesian Ministry of Energy and Mineral Resources One Map (2023)**. AMT1 and AMT15 refer to the location of the AMT observation points. (inset) Map of Indonesia with the red square denotes West Timor, East Nusa Tenggara Province, Indonesia.

and thin-bedded foraminiferal calcilutite. Thin gray shale is also found in these formations (**Charlton, 1989**).

The Bobonaro Formation can be described as a mixture of scaly clay, comprising subangular and disordered angular blocks embedded within a scaly clay matrix (**Charlton et al., 1991**). It is generally reddish brown and green in color but is also, less commonly, gray, black, bright red, and yellow.

The Aitutu Formation is spread widely throughout Timor. It is comprised of both white and gray shale, along with radiolarian calcilutite. This formation is defined as a component of a margin sequence of the Australian continental (**Charlton, 1989**). The Maubise Formation is composed of pink, white and red limestone, often exhibiting dolomitization, and it contains abundant fusulinid and crinoid fragments (**Charlton, 1989**). The Noele Formation overlays the Batuputih Formation. It consists of tuffaceous material, marl interbedded with turbiditic sandstone, and calcilutite. Upwards, it becomes coarser and richer in clastic (**Roosmawati and Harris, 2009**).

Major active faults around the Timor region include the Timor Trough, Semau Fault and the Savu Thrust (**Harris and Major, 2016; Hutchings and Mooney, 2021**). The Timor Trough exhibits megathrust activity, where collision and accretion overprints the subduction process (**Hutchings and Mooney, 2021; Harris, 2011**). The Timor region is recorded as one of the deepest seismicity events in Indonesia (≥ 670 km depth) alongside with the Celebes Sea-Philippines subregion (**Hutchings and Mooney, 2021**). Despite this, the Timor Trough is recognized as the most seismically quiet region of the Banda Arc, though it is acknowledged for its latent capacity to generate significant earthquakes over extended temporal scales (**Coudurier-Curveur et al., 2021**).

The left-lateral transpressional Semau Fault is also known as a primary source of major earthquakes occurring in Timor alongside the Timor Trough. The structural trend is oriented NE–SW, extending from Semau Island to the east of Alor, and is aligned with the structural trend of the currently interpreted fault of this study. **Harris and Major (2016)** characterize the Camplong Fault as a left-lateral strike-slip fault with a NE–SW trend. In contrast, **Soehami et al. (2021)** interpret the Camplong Fault as a thrust fault along the centre part of Timor (see **Figure 1b**). However, both interpretations show similar structural trends. Two other faults, the Babau and Atambua faults are strike-slip faults. The orientation of the them are NW–SE and NE–SW, respectively (**Soehami et al., 2021**). Additionally, the Savu Thrust represents another noteworthy major active fault in the region, originating as a product of the Scott Plateau underthrusting. This fault is situated on the rear of the Sumba-Savu accretionary wedge and has a north-vergence (**Harris et al., 2009**).

3. AMT Data Acquisition and Analysis

3.1. Data Acquisition

A total of 15 AMT observation points were used, depicted as AMT1 to AMT15 in **Figure 1b**. We used AMT data from a PHOENIX MTU5A, which was acquired in May–August 2012. The frequency range is 0.35–10,400 Hz and recorded within two hours for each observation. The average elevation of all observation points was 768.47 meters, with the lowest and highest points being AMT15 (470 m) and AMT11 (1,330 m), respectively.

The profile has an NW–SE orientation and is about 26 km long. The AMT profile passes through a fault zone in the southern section of the East Nusa Tenggara Province. According to the active fault map of Indonesia, released by the Center for Geological Survey, Geological Agency, Ministry of Energy and Mineral Resources of the Republic of Indonesia, this fault is part of the Camplong thrust fault **(Soehaimi et al., 2021)**.

3.1. Data Analysis

We utilized phase tensor as an initial analysis in examining the AMT data, following the methodology described by **Caldwell et al. (2004)**. This analysis allowed us to compute both the regional strike direction and the skew angle (β). The β, in turn, played a crucial role in assessing the study area's dimensionality.

Figure 2 contains the β values for all AMT points across the 26-km-long profile. These β values encompass the entire frequency range, spanning from 0.35 Hz to 10,400 Hz. From AMT1 to AMT15, the β values are dominated by the range of $|\beta| \leq 3°$, except for AMT1 and AMT14 for frequency range 1,000–10,000 Hz and 10–100 Hz, respectively, as indicated by the color scale of **Figure 2**. This indicates that it is feasible to carry out 2-D inversion modelling in our study area. Booker (2014) suggested a range of $|\beta| \leq 3°$ as the threshold for 2-D AMT inversion modelling in a study area based on phase tensor analysis, as introduced by previous study (**Caldwell et al., 2004**).

Figure 3 contains rose diagrams covering all of the AMT observation points at frequencies from 0.1 Hz to 10,0000 Hz. A rose diagram for the entire frequency is also presented in **Figure 3f**. The rose diagram indicates an NE–NW strike direction for the frequency ranges of 0.1–1 Hz, 10−100 Hz, and 100−1,000 Hz, as illustrated in **Figure 3**. On the other hand, the frequency range of 1−10 Hz, 1,000–10,000 Hz, and all frequency are the NE–SE direction.

Figure 1 indicates that the fault line passing the AMT profile runs in an NE–SW direction. Therefore, we applied the NE direction of the regional strike to determine that of the fault line. From the average regional strike direction for all frequencies, we suggest that N25°E be the dominant strike direction. For further analysis, we applied the value of N25°E to rotate the impedance tensor values before applying the inversion modelling.

We also analyzed the induction vectors applying the Parkinson convention (**Parkinson, 1962**), as presented in **Figure 4**. The real part of the induction vectors indicates a conductive zone close to the study area. This analysis is useful if there is a very conductive zone—for example, a sea or lake—close to the study area. In addition, it will also be a sign of the location of a deeper conductor located away from the observational site.

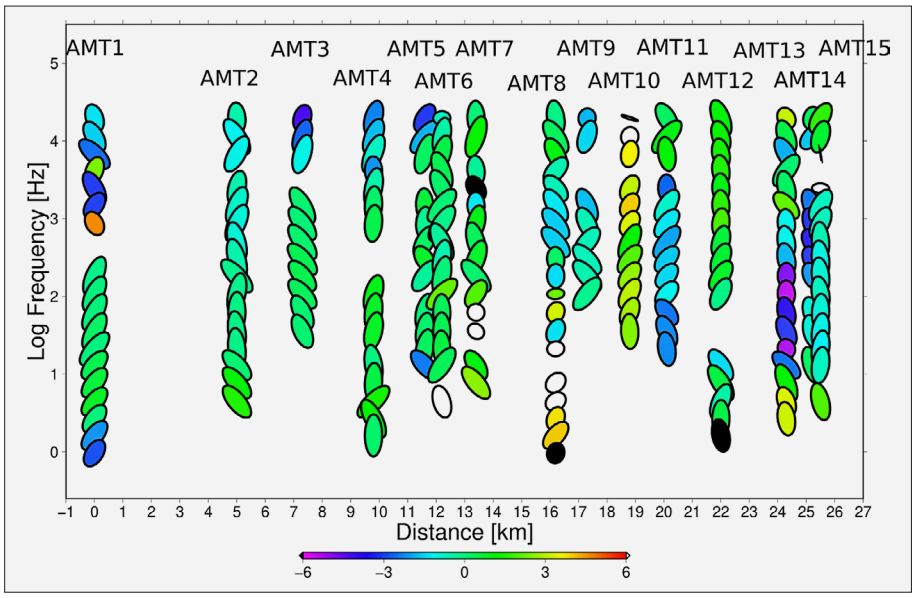

Figure 2. The values of β for all AMT observation points from lower to higher frequencies

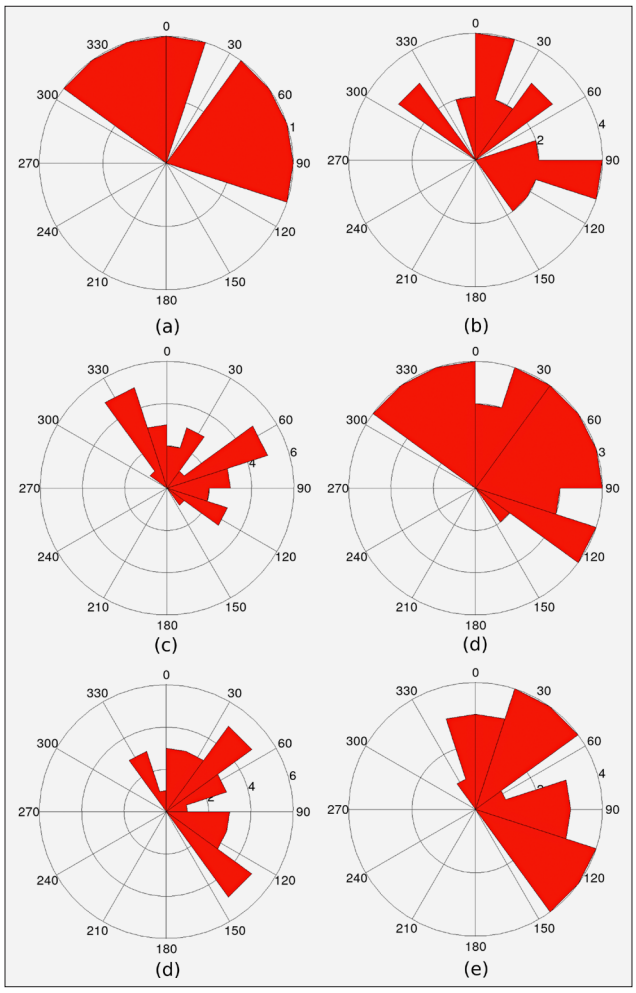

Figure 3. Rose diagrams indicating the study area's regional strike for the frequency ranges of (a) 0.1–1 Hz, (b) 1–10 Hz, (c) 10–100 Hz, (d) 100–1,000 Hz, (e) 1,000–10,000 Hz, and (f) all frequencies

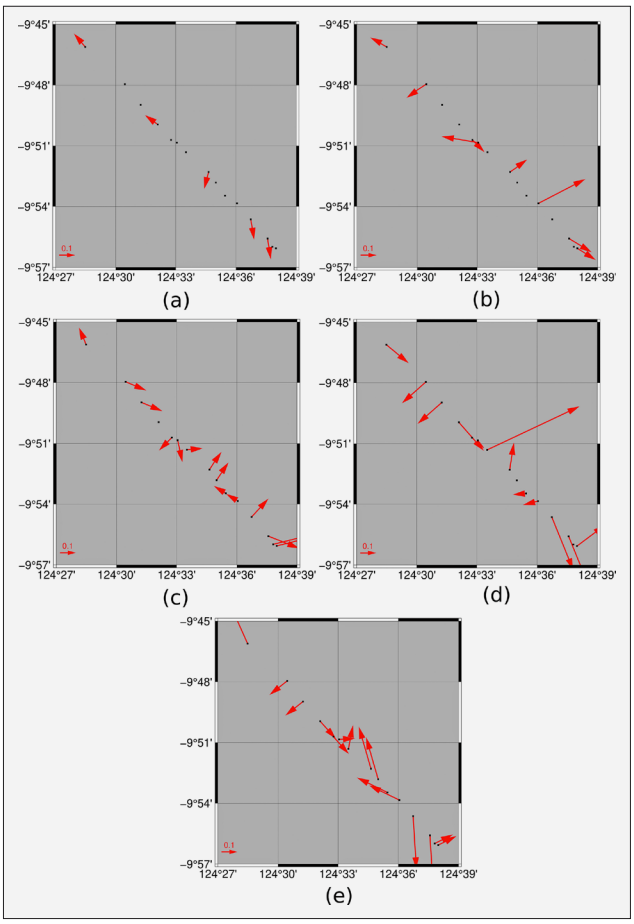

Figure 4. The Parkinson convention induction vectors' real components at frequencies of (a) 1.02 Hz, (b) 11.1 Hz, (c) 115 Hz, (d) 1,100 Hz, (e) 10,399 Hz

As a representative, we plotted the real components of the induction vectors for the frequencies of 1.02 Hz, 11.1 Hz, 115 Hz, 1100 Hz, and 10,399 Hz, as shown in **Figure 4**. The result shows that the orientation of the induction vectors is scattered from the lower to higher frequencies. The research area is situated sufficiently far from the sea and there is no lake in the area surrounding

the AMT profile. **Figure 4** also indicates no deep conductor in the surrounding of the AMT sites.

4. Results

For modelling, we applied the 2-D inversion modelling by **Ogawa and Uchida (1996)**. Prior to conducting the subsurface modelling, we applied a N25°E rotation to the impedance tensor for all AMT points. **Figures 5** and 6 present the phase and apparent resistivity of all AMT points in the transverse magnetic (TM) and transverse electric (TE) modes derived from calculation and observation, respectively.

Figure 5 indicates the same general pattern in the characteristic of the phase and apparent resistivity of all AMT points derived from calculation and observation. The resistivity values are higher in the southeastern part of the AMT profile (near AMT15) than in the northwestern part (near AMT1). The observed apparent resistivity in the TE mode also shows resistive zones close to AMT10 and AMT11 on the near-surface. Near AMT6, AMT 14 and AMT15, the resistive zones appear in the lower frequencies. However, the resistive zone near AMT6 does not emerge in the calculated one.

The TE mode's observed and computed phases present consistent overall characteristics. The phase values in the southeastern part of the AMT profile at a distance of 21–26 km are lower than in the northwestern part of the AMT profile. The lower phase values are indicated close to AMT12, AMT13, AMT14, and AMT15 in the near-surface. The attributes of the observed and computed phases are also similar at the lower frequency.

Figure 6 shows the TM mode's observed and computed phase and apparent resistivity. The similarity of the calculated and observed apparent resistivity is indicated in **Figure 6**. The features of the computed and modelled apparent resistivity for the TM mode are similar to that of the TE mode. The characteristics of the TM mode's calculated and observed apparent resistivity closely resemble those observed for the TE mode for frequency range more than 10 Hz. There is a slight difference for the lower frequency (< 10 Hz). There is a higher resistive value ($\rho \geq 50$ Ωm) near AMT8 and AMT9 in the frequency range less than 10 Hz for TM mode's observed apparent resistivity.

The calculated and observed phases also show a similar general pattern to that of the TE mode. The southeastern part of the AMT profile, close to the distance of 21–26 km, is lower than that of the northwestern part, especially at the frequency range ≥100 Hz. Lower phase value zones exist close to AMT3, AMT5, AMT9, AMT12, AMT13, AMT14, and AMT15 in the near-surface of the study area. These zones are also evident in the TE mode derived from calculation and observation.

Figures 7 and 8 present the phase and apparent resistivity for all AMT points derived from calculation and observation in the TM and TE modes. The red lines indicating the computed phase and apparent resistivity for most of the AMT observation points are fitted with black

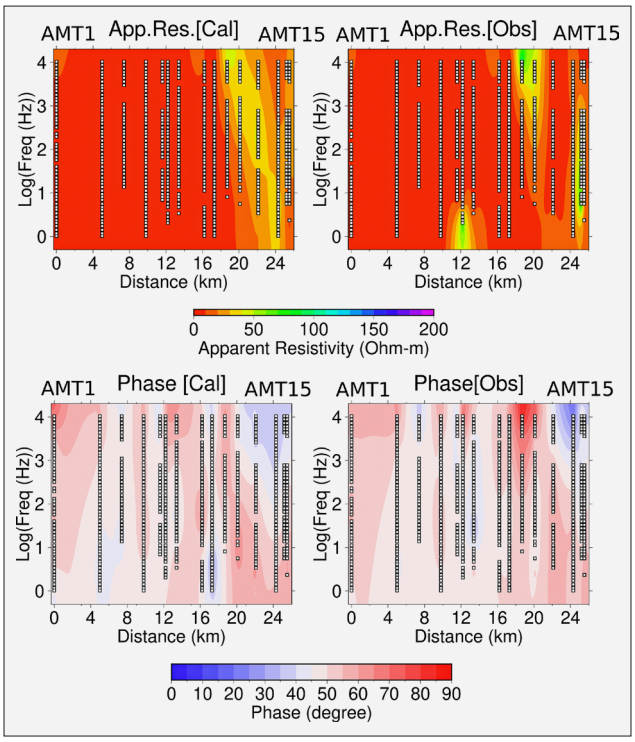

Figure 5. The apparent resistivity and phase of all AMT points in the TE mode derived from calculation and observation

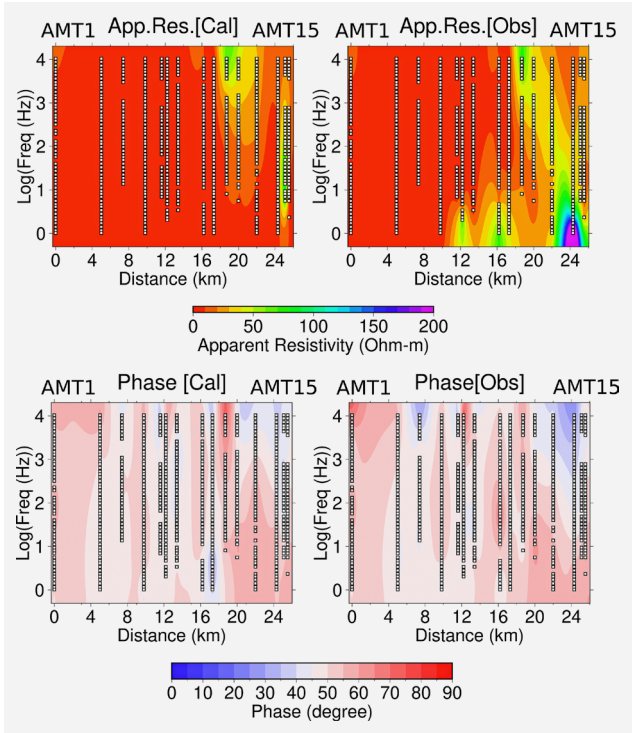

Figure 6. The apparent resistivity and phase of all AMT observation points in the TM mode derived from calculation and observation

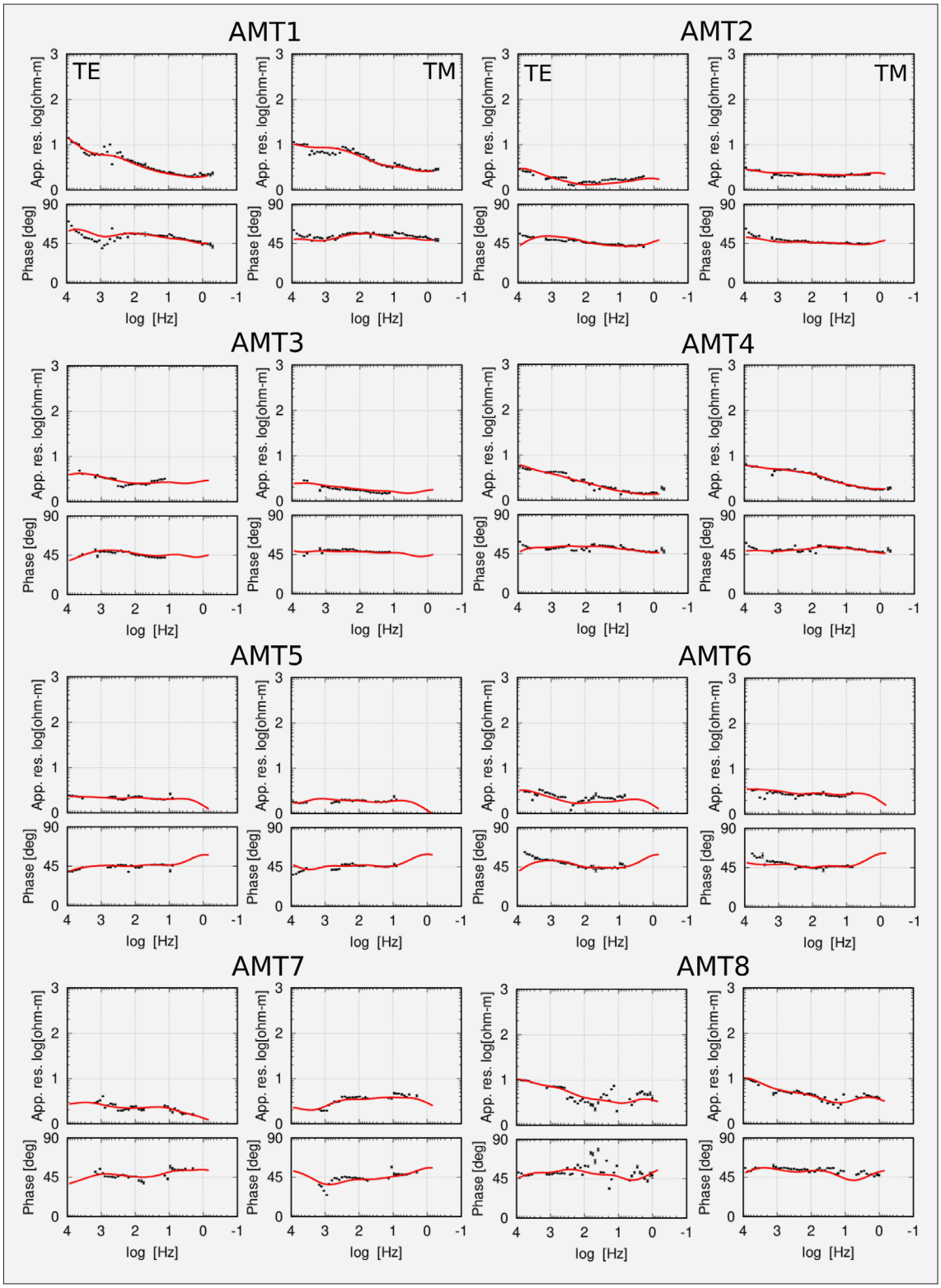

Figure 7. The apparent resistivity and phase for the observation points AMT1 to AMT8 in the TM and TE modes. The red lines represent the computed values, while the black dots represent the observed values.

dots, showing their phase and apparent resistivity observed during the measurement.

These figures indicate that the calculated model could be considered representative of the observed model. Therefore, the subsurface models derived from the 2-D inversion modelling could be regarded as representative models of the subsurface characteristics within the research area along the AMT profile.

We present the electrical subsurface model and its sensitivity model in **Figure 9**. The initial apparent resis-

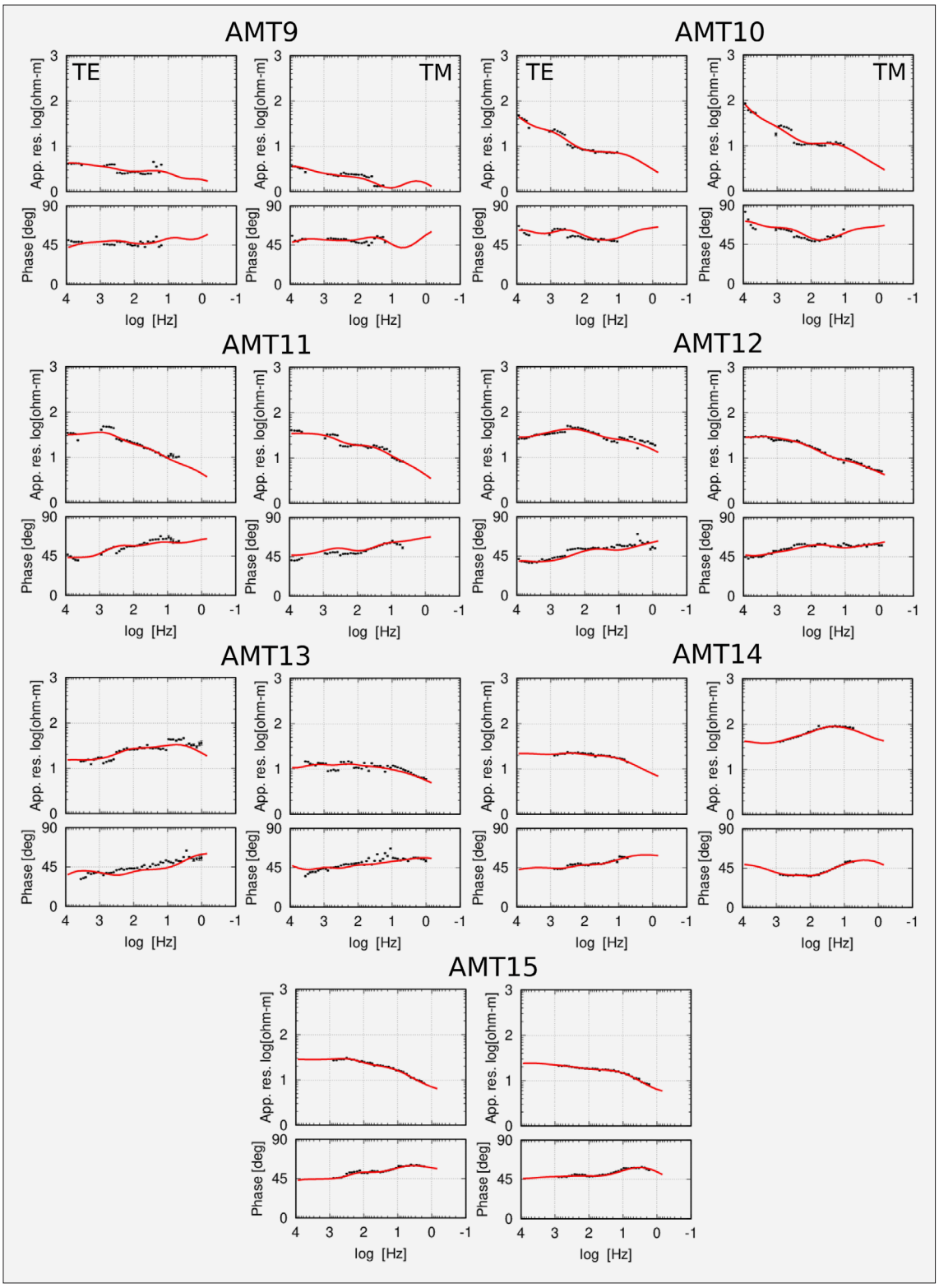

Figure 8. The apparent resistivity and phase for the observation points AMT9 to AMT15 in the TM and TE modes. The red lines represent the computed values, while the black dots represent the observed values.

tivity value of the model is 300 Ωm. We iterated the model 40 times. The root-mean-square (RMS) misfit value of the subsurface model is 1.40.

In the northwestern part of the profile, there are higher resistivity (R1: ρ = 10–50 Ωm) and very low resistivity zones (ρ ≤ 5 Ωm). The very low resistivity zone is near AMT1 from near-surface to the deeper depth. The R1 zone spans from AMT2–AMT7 in the near-surface and goes down to a depth of 2 km near AMT2. In the central part of the AMT profile between AMT7 and AMT8 sites,

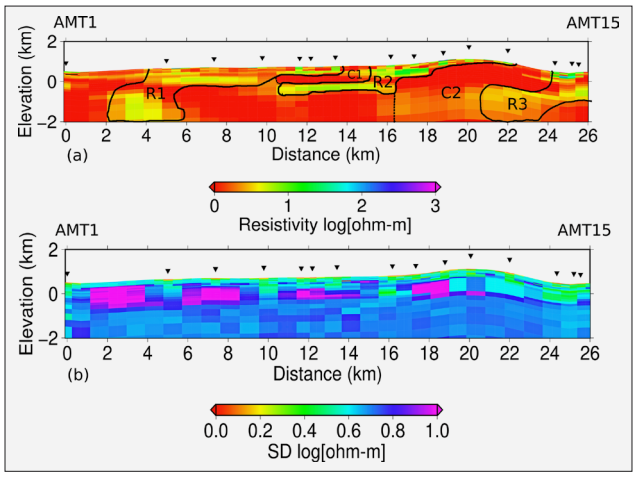

Figure 9. The AMT profile from AMT1 to AMT15. (a) The electrical subsurface model through the AMT profile. (b) The sensitivity model through the AMT profile.

the subsurface model presents a very conductive zone (C1: $\rho \leq 5$ Ωm) from the near-surface to the depth of about 0.5 km. The C1 zone is going below the R1 zone near AMT5–AMT7 and overlays the R2 zone (R2: ρ = 10–50 Ωm). The C1 zone acts as the boundary between the R1 and R2 zones.

Going to the southeastern part of the profile, the subsurface model indicates there are C2 ($\rho \leq 5$ Ωm) and R3 zones (ρ = 5-100 Ωm). The C2 zone is the boundary zone between R2 and R3. The zone is heading downward in the northwestern direction until it reaches a depth of 2 km and overlays the R3 zone at a depth of about 1 km near the AMT11 and AMT12 sites. The R3 zone has a higher apparent resistivity value on the near-surface and its apparent resistivity value decreases while the zone goes downward to a depth of 2 km.

The subsurface model presents two very conductive zones (C1 and C2) as the boundary between the zones

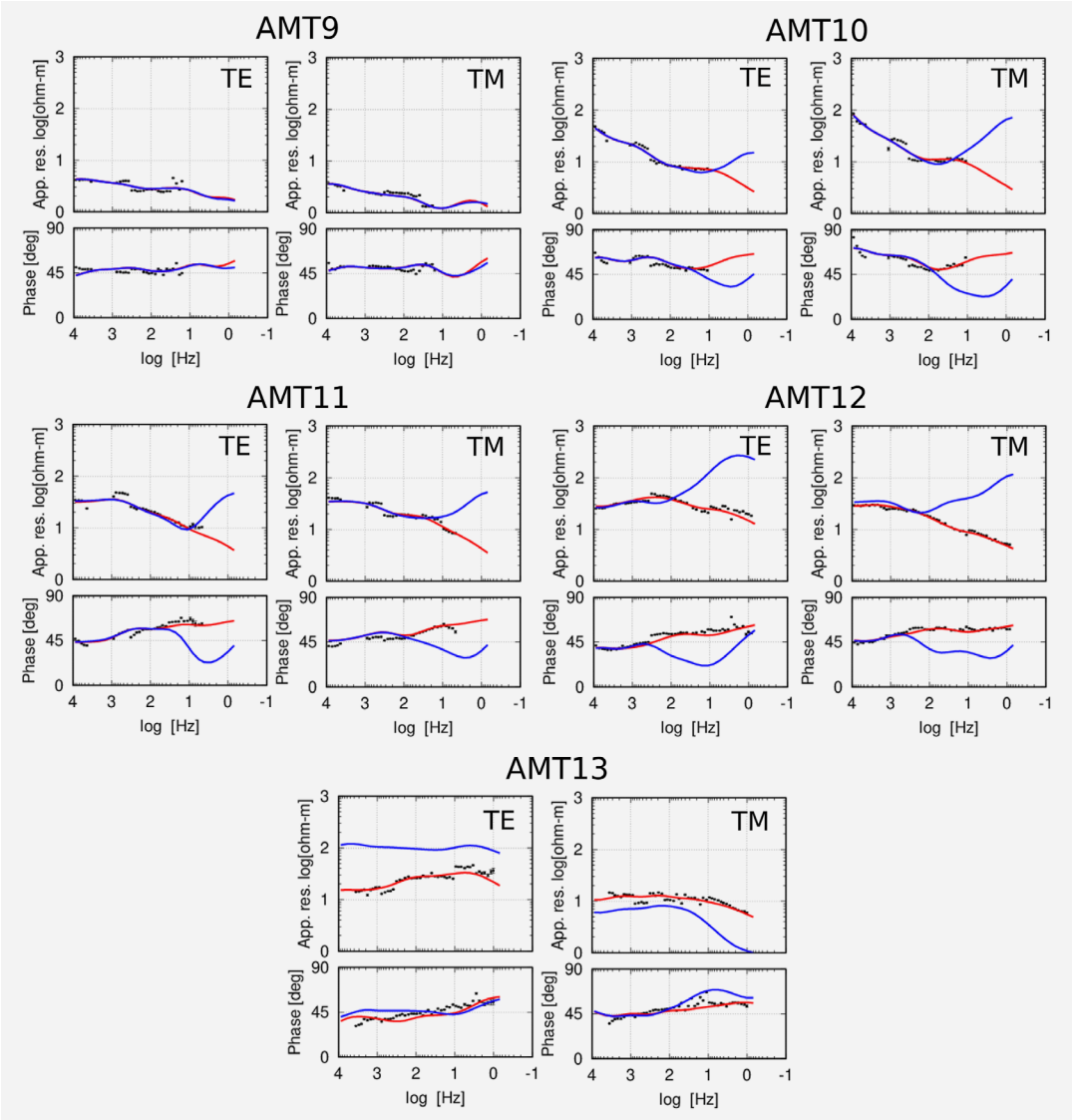

Figure 10. The forward models of apparent resistivity and phase in the TM and TE mode by substituting the C2 value to 500 Ωm. The red lines represent the calculated values, the black dots represent the observed values, and the blue lines represent the forward modelling response

(R1, R2, and R3) which have higher apparent resistivity value compared to its surroundings, as presented in **Figure 9**. However, the R1 zone does not appear in the TE and TM modes of the observed and computed apparent resistivity, as indicated in **Figure 5** and **Figure 6**. In addition, both figures present the C2 as the border between the R2 and R3 zones exist in the southeastern part of the TM and TE modes of the observed and computed apparent resistivity. Therefore, we assume that the C2 is supposed to be the fault zone in this study area.

Figure 9b presents the subsurface model's sensitivity. It was determined by dividing between the upper and lower resistivity values in logarithmic numbers. We can use this sensitivity model to select a reliable subsurface model from the modelling. **Figure 9b** presents the values of the sensitivity model ≤ 0.5 in the near-surface and dominantly about 0.6 in the deeper depth except for the area between AMT1 and AMT2, near AMT3, AMT5, AMT6, AMT9, and AMT10 from the near-surface until a depth of about 0.5 km.

Since there are no AMT observation points between AMT1 and AMT2, AMT2 and AMT3, AMT3 and AMT4, AMT4 and AMT5, or near AMT8, we assume that the higher sensitivity values (≥ 0.5) are caused by the greater distance between the aforementioned observation points and the resolution of the subsurface model in these zones will be lower, as indicated in **Figure 9b**. Therefore, the subsurface model from the 2-D inverse modelling in this study is still valid.

5. Discussion

5.1. Forward modelling

We conducted forward modelling for further analysis to test the validity of the modelling result. In this step, we substituted the resistivity values to 500 Ωm in the C2 zone in **Figure 9a**. The substitution zone runs from the top to a depth of 2 km and covers a horizontal distance from 16.5 km to 24 km. The forward modelling's result is presented in **Figure 10**.

Figure 10 shows the forward modelling conducted for AMT9, AMT10, AMT11, AMT12 and AMT13. It illustrates that when the resistivity value within the zone spanning from AMT9 to AMT12 is set at 500 Ωm, the observed and computed phase and apparent resistivity are out of agreement. The responses of the calculated phase and apparent resistivity after carrying out the forward modelling differ from those obtained after applying the 2-D inverse modelling, as shown by the blue and purple lines in **Figure 10**.

The forward modelling's result indicates that the apparent resistivity values within the region spanning from AMT9 to AMT13, extending from the top to a higher depth, exhibit that the zone is not 500 Ohm-m. It means the C2 zone has the lower apparent resistivity value, as indicated as the conductive zone in the subsurface modelling in **Figure 10**. We can also conclude from **Figure 10** that a conductive boundary (C2) presents in proximity to AMT9, separating the R2 and R3 zones. We suggest that this may be the location of the fault and the conductive boundary (C2) is probably the damaged zone of the fault.

Certain prior research studies have indicated that the border of the resistive and conductive zones is related to the location of the fault region within the study area (**Oshiman et al., 2002; Tank et al., 2005; Kaya et al., 2013; Boonchaisuk et al., 2017; Marti et al., 2020; Usui et al., 2021; Huang et al., 2021; Widarto et al., 2022; Kim et al., 2023**). Furthermore, it was presumed that this boundary would become the site of earthquakes in the future (**Becken et al., 2011; Kaya et al., 2013; Sun et al., 2019; Xu et al., 2019; Zhang et al., 2021**).

5.2. Relationship between electrical subsurface model, seismicity, and geological background

Since the potential fault location suggested by the inverse and forward modelling in the study area's electrical subsurface model differs slightly from that suggested by **Soehaimi et al. (2021)**, we will discuss the relationship between the electrical subsurface model, seismicity, and geological background in this subsection.

We present the earthquakes occurring in the surrounding study area from 1997 to 2022, based on the United States Geological Survey (USGS) catalog (1997–2008) and the Indonesian Agency for Meteorological, Climatological, and Geophysical (BMKG) catalog (2009–2021). All of the earthquakes are presented in **Figure 11a**. The status of all earthquakes from the USGS and BMKG catalogs were reviewed and relocated, respectively (**USGS 2022; Ramdhan et al., 2021**). Their detailed parameters are listed in **Table 1**. We also show the bird view of the study area's geological map which overlays on the subsurface model of the AMT profile in **Figure 11b**.

EQ15 was the earthquake closest to the AMT profile. EQ8, EQ9, EQ12, and EQ15 occurred along the fault trend orientation suggested by **Soehaimi et al. (2021)** and as indicated by the red line in **Figure 11**. However, these occurred at great depth and were possibly triggered by the activity of the Timor Trough. Most of the earthquakes in the region around the research area occurred in the vicinity of the Ofu Formation. This supports the results of the electrical subsurface modelling suggesting that the conductive boundary (C2) is potentially the location of the fault and the C2 zone is probably the damaged zone of the fault.

Geologically, the conductive boundary (C2) may be an elevated section formed as a high horst block of the pre-collisional Australian continental margin. This sequence is capped by the Ofu Formation, which consists of deformed limestones (**Keep and Haig, 2010**) and may be the equivalency of the Borolalo Formation in East Timor (**Charlton and Wall, 1994**) and the Menu Formation in West Timor (**Sawyer et al., 1993**). The de-

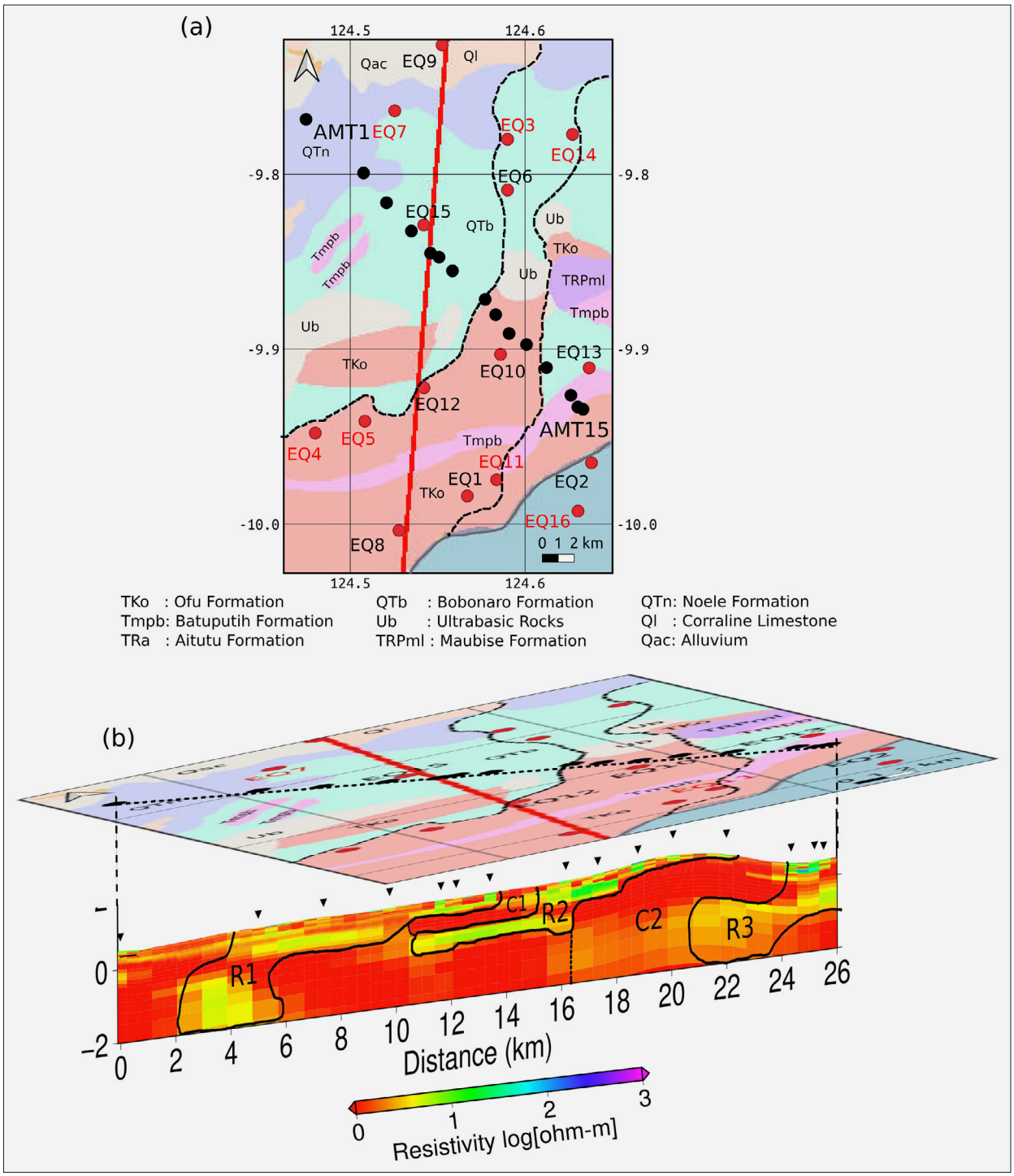

Figure 11. (a) Geological map of study area modified from the **Indonesian Ministry of Energy and Mineral Resources One Map (2023)**. The southwestern part of the Camplong Fault proposed by **Soehaimi et al. (2021)** is marked by a red line. Meanwhile, the orientation of the suggested faults proposed by this study is marked by the black dashed lines. The AMT1 and AMT15 labels indicate the AMT observation points. The red-color label of the earthquakes indicates the earthquakes with a depth less than 15 km, while the black-color label represents the deep-depth earthquakes (depth > 15 km). (b) The bird view of the geological map of the study area overlaying on the subsurface model of the AMT profile.

formation process produced various cracks in the Ofu Formation and led to its very low resistivity value, as indicated by the C2 zone in **Figure 11b**.

The R2 and R3 zones are the Bobonaro Formation, a scaly clay melange comprising subangular and unsorted angular blocks set in a scaly clay matrix (**Charlton et al., 1991**). Notably, the ultrabasic rocks exposed in the area can also be classified as part of the Mutis/Lolotoi Complex. In **Figure 11b**, the ultrabasic rocks appear near the surface of the R2 zone, which is indicated by

Table 1. The detailed parameters of the earthquakes surrounding the study area

No	Date	Longitude (°E)	Latitude (°N)	Depth (km)	Magnitude (Mw)	Catalog
1	14/09/1998	124.567	-9.984	33	4	USGS
2	02/08/2003	124.638	-9.965	33	4.9	USGS
3	11/06/2003	124.590	-9.809	10	5.2	USGS
4	18/07/2005	124.480	-9.948	10	5.4	USGS
5	26/08/2010	124.509	-9.941	4.55	4.6	BMKG
6	23/12/2010	124.590	-9.780	54.5	4.2	USGS
7	14/11/2011	124.525	-9.764	8.43	4.6	BMKG
8	16/12/2012	124.528	-10.004	56.55	4.2	BMKG
9	22/09/2012	124.553	-9.726	41.45	4.3	BMKG
10	23/05/2013	124.586	-9.903	30.40	4.5	USGS
11	18/04/2015	124.584	-9.975	0.62	4.4	BMKG
12	25/10/2016	124.542	-9.922	41.22	3.7	BMKG
13	28/08/2017	124.637	-9.911	39.36	3.4	BMKG
14	06/10/2017	124.627	-9.777	14.02	4.2	BMKG
15	29/01/2018	124.542	-9.829	58.04	3.4	BMKG
16	24/07/2021	124.630	-9.993	11.56	3.8	BMKG

their apparent resistivity value being higher than their surroundings. Although **Rosidi et al. (1979)** classified it as part of a separate formation, **Harris (2006)** summarized that the ultramafic rocks in Timor have been found beneath, above, and intruding through the Mutris/Lolotoi Complex.

Various earthquakes have also occurred at a shallower depth in this location, namely EQ4 (M5.4, depth 10 km), EQ5 (M4.6, depth 4.55 km), and EQ11 (M4.4, depth 0.62 km). Therefore, this indicates that the orientation of the fault trend potentially lies near the boundary between the Ofu and Bobonaro formations, as depicted by the dashed black lines in **Figure 11a**.

Furthermore, additional past shallow earthquake activity and geological and geophysical data are required to better understand the orientation and mechanism of all parts of the Camplong fault in West Timor, East Nusa Tenggara Province. The location of the Camplong Fault must also be mapped precisely in the future because it covers various cities in West Timor, e.g. Kolbane, Oetoeke, Oenai 2, and Nikiniki. Moreover, there are other active faults in West Timor, e.g. the Babau and Atambua faults, which also require further studies on all active faults so that we can mitigate the hazards associated with them. In addition, further research in the future is also still needed by dating ultramafic rock units and various metamorphic massifs in Timor to provide further clarification regarding this enigmatic rock.

5. Conclusions

To investigate the subsurface of the southwestern part of the Camplong active fault in West Timor, East Nusa Tenggara Province, we analyzed 15 AMT data observation points. The AMT profile that passes through the fault line is around 26 km in length and has an NW–SE direction. The analysis of phase tensor indicated that the study area's regional strike is N25°E and it was feasible to apply the 2-D inverse modelling on the AMT data. The inverse modelling results indicate that the electrical subsurface of the study area has a higher resistivity zone (R1: ρ = 10–50 Ωm) in northwestern parts of the AMT profile, a very conductive zone (C1: $\rho \leq 5$ Ωm) and R2 zone (R2: ρ = 10–50 Ωm) in the central part, as well as C2 ($\rho \leq 5$ Ωm) and R3 zones (ρ = 5-100 Ωm) in the southeastern of the AMT profile. The C1 zone acts as the boundary between the R1 and R2 zones, while the C2 zone is the boundary zone between R2 and R3. After comparing the 2D inversion model to the TM and TE modes of the observed and computed apparent resistivity, we assume that the C2 is supposed to be the damaged zone of the fault in this study area. The result from the forward modelling, analysis of seismic activity, and consideration of the geological background further support this result.

Acknowledgement

We express our gratitude to the United States Geological Survey for generously providing the earthquake data. Additionally, we acknowledge partial funding for this study from the National Research and Innovation Agency of the Republic of Indonesia (BRIN).

Funding

The study is funded (in kind) by the National Research and Innovation Agency of the Republic of Indonesia (BRIN).

6. References

Aizawa, K., Koyama, T., Hase, H., Uyeshima, M., Kanda, W., Utsugi, M., Yoshimura, R., Yamaya, Y., Hashimoto, T., Yamazaki, K., Komatsu, S., Watanabe, A., Miyakawa, K., & Ogawa, Y. (2014). Three-dimensional resistivity structure and magma plumbing system of the Kirishima Volcanoes as inferred from broadband magnetotelluric data. Journal of Geophysical Research B: Solid Earth, 119(1), 198–215. https://doi.org/10.1002/2013JB010682

Barber, A. J. (1978). Structural interpretations of the island of Timor eastern Indonesia. Proceeding of the Southeast Asian Petroleum Exploration Society, 4, 9–21.

Barber, A. J. and Brown, K. (1988). Mud diapirism: the origin of melanges in accretionary complexes? Geology Today, 4(3), 89–94. https://doi.org/10.1111/j.1365-2451.1988.tb00562.x

Becken, M., Ritter, O., Bedrosian, P. A., & Weckmann, U. (2011). Correlation between deep fuids, tremor and creep along the central San Andreas fault. Nature, 480, 87–90. https://doi.org/10.1038/nature10609

Bock, Y., Prawirodirdjo, L., Genrich, J. F., Stevens, C. W., McCaffrey, R., Subarya, C., Puntodewo, S. S. O., & Calais, E. (2003). Crustal motion in Indonesia from Global Positioning System measurements. Journal of Geophysical Research, 108(B8), 2367. https://doi.org/10.1029/2001JB000324

Booker, J. R. (2014). The magnetotelluric phase tensor: a critical review. Surveys in Geophysics, 35, 7–40. https://doi.org/10.1007/s10712-013-9234-2

Boonchaisuk, S., Noisagool, S., Amatyakul, P., Rung-Arunwan, T., Vachiratienchai, C., & Siripunvaraporn, W. (2017). 3-D magnetotelluric imaging of the Phayao Fault Zone, Northern Thailand: Evidence for saline fluid in the source region of the 2014 Chiang Rai earthquake. Journal of Asian Earth Scienses, 147, 210–221. https://doi.org/10.1016/j.jseaes.2017.07.034

Caldwell, T. G., Bibby, H. M., & Brown, C. (2004). The magnetotelluric phase tensor. Geophysical Journal International, 158(2), 457–469. https://doi.org/10.1111/j.1365-246X.2004.02281.x

Chamalaun, F. H. and Grady, A. E. (1978). The tectonic development of Timor: A new model and its implications for petroleum exploration. Australian Petroleum Production & Exploration Association (APPEA) Journal, 18(1), 102–108. https://doi.org/10.1071/AJ77012

Charlton, T. R. (1989). Stratigraphic correlation across an arc-continent collision zone: Timor and the Australian Northwest Shelf. Australian Journal of Earth Sciences, 36(2), 263–274. https://doi.org/10.1080/08120098908729485

Charlton, T. R., Barber, A. J., & Barkham, S. T. (1991). The structural evolution of the Timor collision complex, eastern Indonesia. Journal of Structural Geology 13(5): 489–500. https://doi.org/10.1016/0191-8141(91)90039-L

Charltony, T. R. and Wall, D. (1994). New biostratigraphic results from the Kolbano area, southern West Timor: Implications for the Mesozoic—Tertiary stratigraphy of Timor. Journal of Southeast Asian Earth Sciences, 9(1–2), 113–122. https://doi.org/10.1016/0743-9547(94)90069-8

Charlton, T. R. (2002). The petroleum potential of West Timor. 28th Annual Convention Proceedings, 1, 301–307

Charlton, T. R. and Titu-Eki, A.T. (2023) 'Banda Terrane' Basement and Cover in the Noil Meto River Section, Southern West Timor (Timor Barat, Nusa Tenggara Timur, Indonesia). Indonesian Journal of Sedimentary Geology, 49(1), 1–24

Coudurier-Curveur, A., Singh, S. C., Deighton, I. (2021). Timor Collision Front Segmentation Reveals Potential for Great Earthquakes in the Western Outer Banda Arc, Eastern Indonesia. Frontrier of Earth Science, 9, 640928. https://doi.org/10.3389/feart.2021.640928

Daud, Y., Nuqramadha, W. A., Fitriastuti, A., Darmawan, D., Fahmi, F., Tifani, M. A., Tarmidi, S., Iskandar, C., & Ibrahim, R. F. (2023). Investigation of deep-seated heat source through 3-D Magnetotelluric inversion in Arjuno-Welirang volcanic complex (East Java). Geothermics, 113, 102768. https://doi.org/10.1016/j.geothermics.2023.102768

DeMets, C., Gordon, R. G., & Argus, D. F. (2010). Geologically current plate motions. Geophysical Journal International, 181(1), 1–80. https://doi.org/10.1111/j.1365-246X.2009.04491.x

Febriani, F., Widarto, D. S., Gaffar, E. Z., Nasution, A., Grandis, H., Anggono, T., & Syuhada, S. (2019). Magnetotelluric investigation for imaging the subsurface geoelectrical feature of the prospective Sembalun-Propok geothermal zone, Indonesia. Arabian Journal of Geosciences, 12, 1–18. https://doi.org/10.1007/s12517-019-4723-3

Harris, R. (2006). Rise and fall of the Eastern Great Indonesian arc recorded by the assembly, dispersion and accretion of the Banda Terrane, Timor. Gondwana Research, 10(3-4), 207-231. https://doi.org/10.1016/j.gr.2006.05.010

Harris, R., Vorkink, M. W., Prasetyadi, C., Zobell, E., Roosmawati, N., & Apthorpe, M. (2009). Transition from subduction to arc-continent collision: Geologic and neotectonic evolution of Savu Island, Indonesia. Geosphere, 5(3), 152–171. https://doi.org/10.1130/GES00209.1

Harris, R. (2011). The nature of the Banda arc-continent collision in the Timor region. *Arc continent collision*. *Frontiers in Earth Sciences. Springer, Berlin, Heidelberg*, 163-211. https://doi.org/10.1007/978-3-540-88558-0_7

Harris, R. and Major, J. (2016). Waves of destruction in the East Indies: the Wichmann catalogue of earthquakes and tsunami in the Indonesian region from 1538 to 1877. Geological Society Special Publication, 441, 9–46. https://doi.org/10.1144/SP441.2

Honkura, Y., Isikara, A. M., Oshiman, N., Ito, A., Üçer, B., Baris, S., Tuncer, M. K., Matsushima, M., Pektas, R., Celik, C., Tank, S. B., Takahashi, F., Nakanishi, M., Yoshimura, R., Ikeda, Y., & Komut, T. (2000). Preliminary results of multidisciplinary observations before, during and after the Kocaeli (Izmit) earthquake in the western part of the North Anatolian Fault Zone. Earth, Planets and Space, 52, 293–298. https://doi.org/10.1186/BF03351638

Huang, J., Ma, C., & Sun, Y. (2021). 2D magnetotelluric forward modelling for deeb buried water-rich fault and its application. Journal of Applied Geophysics, 192, 104403. https://doi.org/10.1016/j.jappgeo.2021.104403

Hutchings, S. J. and Mooney, W. D. (2021). The seismicity of Indonesia and tectonic implications. Geochemistry, Geophysics, Geosystem, 22(9):e2021GC009812. https://doi.org/10.1029/2021GC009812

Indonesian Ministry of Energy and Mineral Resources One Map, 2023, https://geoportal.esdm.go.id/geologi/. Accessed 10 August 2023

Ingham, M. R., Bibby, H. M., Heise, W., Jones, K. A., Cairns, P., Dravitzki, S., Bennie, S. L., Caldwell, T. G., & Ogawa, Y. (2009). A magnetotelluric study of Mount Ruapehu volcano, New Zealand. Geophysical Journal International 179: 887–904. https://doi.org/10.1111/j.1365-246X.2009.04317.x

Junian, W. E. and Grandis, H. (2023). Hybrid particle swarm optimization and grey wolf optimizer algorithm for Controlled Source Audio-frequency Magnetotellurics (CSAMT) one-dimensional inversion modelling. Rudarsko-geološko-naftni zbornik, 38(3), 65–80. https://doi.org/10.17794/rgn.2023.3.6

Jacobson, M.I. and Sani, K. (1993). Guidebook of Indonesian Petroleum Association Post Convention Field Trip 1993 West Timor, Nusa Tenggara Timur. Indonesian Petroleum Association, Indonesia.

Kaya, T., Kasaya, T., Tank, S. B., Ogawa, Y., Tunçer, M. K., Oshiman, N., Honkura, Y., & Matsushima, M. (2013). Electrical characterization of the North anatolian fault zone underneath the Marmara Sea, Turkey by ocean bottom magnetotellurics. Geophysical Journal International, 193(2), 664–677. https://doi.org/10.1093/gji/ggt025

Keep, M., Haig, & D. W. (2010). Deformation and exhumation in Timor: Distinct stages of a young orogeny. Tectonophysics, 483(1–2), 93–111. https://doi.org/10.1016/j.tecto.2009.11.018

Kim, K., Oh, S., Kwon, H. S., Lee, S. K., & Chung, H. (2023). Two-dimensional interpretation of audio-magnetotelluric data around the epicenter distribution of the 2016 Gyeongju earthquake (M L 5.8), Korea. Geosciences Journal. https://doi.org/10.1007/s12303-023-0016-7

Martí, A., Queralt, P., Marcuello, A., Ledo, J., Rodríguez-Escudero, E., Martínez-Díaz, J. J., Campanyà, J., & Meqbel, N. (2020). Magnetotelluric characterization of the Alhama de Murcia Fault (Eastern Betics, Spain) and study of magnetotelluric interstation impedance inversion. Earth, Planets and Space 72, 16. https://doi.org/10.1186/s40623-020-1143–2

Newman, G. A., Gasperikova, E., Hoversten, G. M., & Wannamaker, P. E. (2008). Three-dimensional magnetotelluric characterization of Coso geothermal field. Geothermics, 37, 369–399. https://doi.org/10.1016/j.geothermics.2008.02.006

Ogawa, Y. and Uchida, T. (1996). A two-dimensional magnetotelluric inversion assuming Gaussian static shift. Geophysical Journal International 126(1), 69–76. https://doi.org/10.1111/j.1365-246X.1996.tb05267.x

Ogawa, Y., Mishina, M., Goto, T., Satoh, H., Oshiman, N., Kasaya, T., Takahashi, Y., Nishitani, T., Sakanaka, S., Uyeshima, M., Takahashi, Y., Honkura, Y., & Matsushima, M. (2001). Magnetotelluric imaging of fluids in intraplate earthquake zones, NE Japan back arc. Geophysical Research Letters, 28, 3741–3744. https://doi.org/10.1029/2001GL013269

Oshiman, N., Yoshimura, R., Kasaya, T., Honkura, Y., Matsushima, M., Baris, S., Celik, C., Tuncer, M. K., & Isikara, A. M. (2002) Deep resistivity structure around the fault associated with the 1999 Kocaeli earthquake, Turkey, *Seismotectonics in Convergent Plate Boundary. Terra Scientific Publishing Company, Japan*, 293–303.

Parkinson, W. D. (1962). The infuence of continents and oceans on geomagnetic variations. Geophysical Journal International, 6(4), 441–449. https://doi.org/10.1111/j.1365-246X.1962.tb02992.x

Powell, D. E. (1976) The geological evolution of the continental margin of Northwest Australia. Journal of Australian Petroleum Exploration Association, 16, 13–23. https://doi.org/10.1071/AJ75002

Ramdhan, M., Priyobudi, Imananta, R.T., Muzli, Supendi, P., Perdana, Y. H., Nugraha, J., Jatnika, J., Ali, Y. H., Panjaitan, A. L., Nugraha, M. F., Kristyawan, S., Sembiring, A. S., Setyahagi, A. R., & Yogaswara, D. S. (2021). *Indonesia's Earthquake Catalog: Hypocenter Relocation and Its Tectonic Implication, Center of Earthquake and Tsunami. Indonesian Agency for Meteorological, Climatological and Geophysical (BMKG)* (in Bahasa)

Rosidi, H. M. D., Suwitodirdjo, K., & Tjokosopoetro, S. (1979). Geological map of Kupang-Atambua quadrangle, Timor Scale 1: 250 000. Indonesian Geological Research Development Centre, Bandung, Indonesia

Roosmawati, N. and Harris, R. (2009). Surface uplift history of the incipient Banda arc-continent collision: Geology and synorogenic foraminifera of Rote and Savu Islands, Indonesia. Tectonophysics, 479(1–2), 95–110. https://doi.org/10.1016/j.tecto.2009.04.009.

Sawyer, R. K., Sani, K., & Brown, S. (1993). The stratigraphy and sedimentology of West Timor, Indonesia. Proceeding of Indonesian Petroleum Association 22nd Annual Convention. https://www.ipa.or.id/en/publications/the-stratigraphy-and-sedimentology-of-west-timor-indonesia. Accessed 17 September 2024

Simpson, F. and Bahr, K. (2005). *Practical magnetotellurics. Cambridge University Press*, *Cambridge*

Soehaimi, A., Sopyan, Y., Ma'mur, & Agustin, F. (2021). Active Fault Map in Indonesia Scale 1:5.000.000. Center for Geological Survey, Geological Agency Ministry Energy and Mineral Resources.

Špičák, A., Matějková, R., & Vaněk, J. (2013). Seismic response to recent tectonic processes in the Banda Arc region. Journal of Asian Earth Sciences, 64, 1–13. https://doi.org/10.1016/j.jseaes.2012.11.014

Sun, X., Zhan, Y., Zhao, L., Chen, X., Sun, J., Li, C., & Cui, T., Han, J. (2019). Electrical structure of the Kunlun-Qinling fault system, northeastern Tibetan Plateau, inferred from 3-D inversion of magnetotelluric data. Journal of Asian Earth Sciences, 181, 103910. https://doi.org/10.1016/j.jseaes.2019.103910

Tank, S. B., Honkura, Y., Ogawa, Y., Matsushima, M., Oshiman, N., Tunçer, M. K., Çelik, C., Tolak, E., & Işıkara, A.

M. (2005). Magnetotelluric imaging of the fault rupture area of the 1999 Izmit (Turkey) earthquake. Physics of the Earth and Planetary Interiors, 150(1–3), 213–225. https://doi.org/10.1016/j.pepi.2004.08.033

Usui, Y., Uyeshima, M., Ogawa, T., Yoshimura, R., Oshiman, N., Yamaguchi, S., Toh, H., Murakami, H., Aizawa, K., Tanbo, T., Ogawa, Y., Nishitani, T., Sakanaka, S., Mishina, M., Satoh, H., Goto, T., Kasaya, T., Mogi, T., Yamaya, Y., Shiozaki, I., & Honkura, Y. (2021). Electrical resistivity structure around the Atotsugawa fault, central Japan, revealed by a new 2-D inversion method combining wideband-MT and Network-MT data sets. Journal of Geophysical Research B: Solid Earth 126(4):e2020JB020904. https://doi.org/10.1029/2020JB02090

USGS, https://earthquake.usgs.gov/earthquakes/search/. Accessed 25 December 2022

Widarto, D. S., Febriani, F., Nurdiyanto, B., Syuhada, S., Anggono, T., Dewi, C. N., Prasetio, & A. D. (2022) Magnetotelluric resistivity imaging of the Baribis fault zone's Majalengka segment in West Java, Indonesia. Acta Geodaetica et Geophysica 57:177–194. https://doi.org/10.1007/s40328-022-00372-w

Varekam, J. C., Van Bergen, M. J., Vroon, P. Z., Poorter, R. P. E., Wirakusumah, A. D., Erfan, R., Suharyono, K., & Sriwana, T. (1989). Volcanism and tectonics in the eastern Sunda Arc, Indonesia. Netherlands Journal of Sea Research, 24(2–3), 303–312. https://doi.org/10.1016/0077-7579(89)90156-7

Villeneuve, M., Bellon, H., Martini, R., Harsolumakso, A., & Cornee, J. J. (2013). West Timor: a key for the eastern Indonesian geodynamic evolution. Bulletin de la Societe Geologique de France 184(6), 569–582. https://doi.org/10.2113/gssgfbull.184.6.569

Vozoff, K. (1991). The Magnetotelluric method. *Electromagnetic Methods in Applied Geophysic vol 2B*, *Society of Exploration Geophyscist, Tulsa, Oklahoma*, 641–711

Xu, Z. M., Tang, J. T., Li, G., Xin, H. C., Xu, Z. J., Tany, X. P., & Li, J. (2019). Groundwater resources survey of Tongchuan city using audio magnetotelluric method. Applied Geophysics 17, 660-671. https://doi.org/10.1007/s11770-018-0709-2

Yamaya, Y., Alanis, P. K. B., Takeuchi, A., Cordon, Jr. J. M., Mogi, T., Hashimoto, T., Sasai, Y., & Nagao, T. (2013). A large hydrothermal reservoir beneath Taal Volcano (Philippines) revealed by magnetotelluric resistivity survey: 2D resistivity modeling. Bulletin og Volcanology, 75, 729. https://doi.org/10.1007/s00445-013-0729-y

Zhang, S., Yu, N., Wang, E., Li, D., Li, R., & Liu, Y. (2021). The seismogenic structure and dynamic environment of Wulong Ms 5.0 earthquake revealed by magnetotelluric imaging. Tectonophysics, 811, 228867. https://doi.org/10.1016/j.tecto.2021.228867

SAŽETAK

Istraživanje podzemlja jugozapadnoga dijela aktivnoga rasjeda Camplong, Zapadni Timor, Indonezija, primjenom inverzije audiofrekventnih magnetotelurskih podataka

Geološki u Zapadnome Timoru u pokrajini Istočna Nusa Tenggara (NTT) u Indoneziji postoje tri aktivna rasjeda, i to rasjedi Babau, Camplong i Atambua. Podatci audiofrekventnoga magnetotelurskog (AMT) mjerenja korišteni su za modeliranje geoelektričnoga podzemlja jugozapadnoga dijela rasjeda Camplong. AMT profil, koji se sastojao od 15 AMT promatračkih točaka na duljini od 26 km u smjeru SZ-JI, podvrgnut je analizi faznoga tenzora. Rezultati sugeriraju da proučavano područje ima regionalni smjer N25°E te da je 2D inverzno modeliranje na AMT profilu bilo moguće. Rezultat inverznoga modeliranja upućuje na prisutnost dviju vodljivih granica (C1: $\rho \leq 5$ Ωm i C2: $\rho \leq 5$ Ωm) u središnjemu i jugoistočnome dijelu AMT profila koji odvaja zone R1 ($\rho = 10 - 50$ Ωm) i R2 ($\rho = 10 - 50$ Ωm), kao i R2 i R3 ($\rho = 5 - 100$ Ωm). R1, R2 i R3 nalaze se u sjeverozapadnome, središnjemu i jugoistočnome dijelu. Smatramo da je C2 moguća oštećena zona rasjeda u ovome području istraživanja. Također smo proveli direktno modeliranje i ispitali seizmičku aktivnost i geološku pozadinu, čiji su rezultati usklađeni s inverznim modeliranjem.

Ključne riječi:
rasjedna zona, potres, audiofrekventna magnetotelurika, istočna Nusa Tenggara, model podzemlja

Author's contribution

Febty Febriani (Dr): Conceptualization, methodology, audio-frequency magnetotelluric data validation and analysis, audio-frequency magnetotelluric data curation, writing (original draft), writing (review and editing), and visualization. **Cinantya Nirmala Dewi** (M.Sc): Methodology, audio-frequency magnetotelluric data curation, and writing (review and editing). **Gusti Muhammad Lucki Junursyah** (M.Sc): Providing audio-frequency magnetotelluric data, audio-frequency magnetotelluric data curation, and writing (review and editing). **Titi Anggono** (Dr)**, Syuhada** (Dr)**, Mohamad Ramdhan** (Dr)**, Faiz Muttaqy** (Dr)**, Mohammad Hasib** (Dr) and **Wiko Setyonegoro** (M.Sc): Writing (original draft), seismical data curation, and writing (review and editing). **Herry Zardak Kotta** (Dr) and **Aditya Dwi Prasetio** (M.Sc): Geological data curation, Geological data interpretation, and writing (review and editing).
All authors read and accepted the final form of the manuscript.